NANO LETTERS

Access provided by MIT Libraries

Subscriber access provided by MIT Libraries

Communication

Freestanding organic charge-transfer conformal electronics

Zhuolei Zhang, Huashan Li, Richards Miller, Hans Malissa, Shirin Jamali, Christoph Boehme, Jeffrey C. Grossman, and Shenqiang Ren

Nano Lett., **Just Accepted Manuscript** • DOI: 10.1021/acs.nanolett.8b01342 • Publication Date (Web): 01 Jun 2018

Downloaded from http://pubs.acs.org on June 12, 2018

Just Accepted

"Just Accepted" manuscripts have been peer-reviewed and accepted for publication. They are posted online prior to technical editing, formatting for publication and author proofing. The American Chemical Society provides "Just Accepted" as a service to the research community to expedite the dissemination of scientific material as soon as possible after acceptance. "Just Accepted" manuscripts appear in full in PDF format accompanied by an HTML abstract. "Just Accepted" manuscripts have been fully peer reviewed, but should not be considered the official version of record. They are citable by the Digital Object Identifier (DOI®). "Just Accepted" is an optional service offered to authors. Therefore, the "Just Accepted" Web site may not include all articles that will be published in the journal. After a manuscript is technically edited and formatted, it will be removed from the "Just Accepted" Web site and published as an ASAP article. Note that technical editing may introduce minor changes to the manuscript text and/or graphics which could affect content, and all legal disclaimers and ethical guidelines that apply to the journal pertain. ACS cannot be held responsible for errors or consequences arising from the use of information contained in these "Just Accepted" manuscripts.

ACS Publications

is published by the American Chemical Society. 1155 Sixteenth Street N.W., Washington, DC 20036

Published by American Chemical Society. Copyright © American Chemical Society. However, no copyright claim is made to original U.S. Government works, or works produced by employees of any Commonwealth realm Crown government in the course of their duties.

Freestanding organic charge-transfer conformal electronics

Zhuolei Zhang,[1, 2, +] Huashan Li,[3, 4+] Richards Miller,[5] Hans Malissa,[5] Shirin Jamali,[5] Christoph Boehme,[5] Jeffrey C. Grossman,[4,*] and Shenqiang Ren[1,*]

[1] Department of Mechanical and Aerospace Engineering, University at Buffalo, The State University of New York, Buffalo, NY 14260, USA

[2] Research and Education in Energy, Environment & Water (RENEW), University at Buffalo, The State University of New York, Buffalo, NY 14260, USA

[3]Sino-French Institute of Nuclear Engineering & Technology, Sun Yat-Sen University, Tang-Jia-Wan, Zhuhai City, Guangdong Province, 519-082, PR China

[4]Department of Materials Science and Engineering, Massachusetts Institute of Technology, Cambridge, Massachusetts 02139 USA

[5]Department of Physics and Astronomy, University of Utah, 115 South 1400 East, Salt Lake City, Utah 84112-0830, USA

+ Equal contribution;

Email: jcg@mit.edu; shenren@buffalo.edu

Abstract

Wearable conformal electronics are essential components for next-generation humanlike sensing devices that can accurately respond to external stimuli in non-planar and dynamic surfaces. However, to explore this potential, it is indispensable to achieve the desired level of deformability and charge transport mobility in strain-accommodating soft semiconductors. Here we show pseudo-two-dimensional freestanding conjugated polymer heterojunction nanosheets integrated into substrate-free conformal electronics, owing to their exceptional crystalline controlled charge transport and high level of mechanical strength. These freestanding and mechanical robust polymer nanosheets can be adapted into a variety of artificial structured surfaces such as fibers, squares, circles, etc, which produce large-area stretchable conformal charge-transfer sensors for real-time static and dynamic monitoring.

Keywords: Pseudo-2D, Charge Transfer, Organic Films, Mechanical Strength, Conformal Electronics

The emergence of wearable and implantable electronics has stimulated significant interest in conjugated polymers that are lightweight, flexible and stretchable, for applications such as organic integrated circuits,[1-2] displays,[3] and solar cells.[4-5] However, it remains a key challenge to realize the simultaneous demonstration of outstanding electronic performance and mechanical robustness in conjugated polymers.[5] The competition between these two properties arises because high charge mobility polymers tend to be brittle from the rigid π-conjugated chains and high degrees of crystallinity, which is mutually incompatible to deformability, while the amorphous and flexible counterparts possess low electronic performance. Such competition can lead to flexible and stretchable yet low-performance devices or high-performance ones that cannot accommodate the strain (leading in turn to delamination, cracking, etc). A thickness reduction to achieve pseudo-two-dimensional (pseudo-2D) crystalline polymer nanosheets holds great promise to address this challenge of mutual exclusivity of electronic and mechanical performance, due to a combination of enhanced adaptability with irregular surfaces and induced nanoconfinement that can substantially affect the polymer properties via finite-size effects and interfacial engineering.[6-8]

Nanoconfinement of polymers with the thickness below 1000 nm has been demonstrated to enhance polymer chain dynamics and prevent crack propagation,[8-11] which results in the variation of properties such as the glass transition temperature, Young's modulus, and ductility.[10-13,8-9] In addition, nanoconfinement has also been

explored as a potential means to tune electronic properties of polymers by manipulating chain alignment,[14-15] as shown in the enhanced anisotropy and mobility in organic transistors.[14] In pseudo-2D crystalline conjugated polymers, both mechanical strength and charge transport would benefit from the increased domain alignment by nanoconfinement effects orthogonal to the polymer sheets. Such crystalline polymers to external stimuli are governed by the variations of π-π stacking rather than polymer diffusion or chemical bond breaking, and therefore the ensemble exhibits intrinsic advantages of fast response time, low threshold, little hysteresis, and high cycling capability.

Here, we report that pseudo-2D freestanding polythiophene-fullerene (PthFu) crystalline nanosheets exhibit a rare combination of high level of mechanical robustness and charge transport mobility, which is enabled by pseudo-2D nanoconfinement and charge-transfer interactions as identified by both experimental and computational analysis. The mechanical and electronic properties of pseudo-2D PthFu nanosheets are governed by the electron coupling strength between π-stacking units and reflect the collective effects of all crystalline domains under external perturbation. These effects are achieved because of the high degree of crystallinity and domain alignment driven by the geometrical confinement effects. The introduction of a pseudo-2D architecture in crystalline polymer materials influences a range of electronic, optical and spin-dependent properties mainly by tuning the interfacial charge-transfer interactions between neighboring conjugation

units, ordering of the entire film, and the proportion of surface areas. The intensive suppression of disorder by imposing spatial constraints within a nanosheet architecture has the potential to dramatically increase the synergy between crystalline domains, which paves an avenue to harvest the intrinsic sensitivity of molecular coupling to interfacial structure. Such promise can be illustrated by probing the responses of the PthFu nanosheets to various external stimuli. This contributes to the development of substrate-free conformal sensors based on the sensitivity of electron coupling to π-π stacking configuration, with the potential of advanced functionalization revealed by the embedded photovoltaic effect.

The inherent softness, high absorption coefficient and carrier mobility of pseudo-2D PthFu nanosheet make such a charge-transfer material especially attractive for organic electronics.[16-18] We develop a new water-air interfacial growth technique to control the crystallization and molecular packing of the PthFu blends, considering that an inert and halogenated solvent environment is currently required for the entire process. When the PthFu solution spreads spontaneously and rapidly onto the water surface due to the Marangoni effect,[19] the water, PthFu surface and the surrounding vapor atmosphere all come into play.[20-21] The extent of solution spreading on water is estimated by the Neumann triangle of force balance which is described by the spreading coefficient $S=\gamma_{WG}-\gamma_{GO}-\gamma_{WO}$, where γ_{WG}, γ_{GO}, and γ_{WO} represent the surface tension of the water/air, PthFu/air, and water/PthFu interfaces. If S is positive, the PthFu solution tends to spontaneously spread over the aqueous

surface and form a uniform pseudo-2D polymer nanosheet (Fig.S1). Otherwise, the spreading is inhibited with the PthFu oil drop preserved (Fig.S1c).[22-23] We select the mixed solvents (1:4=1,2-dichlorobenzene:toluene) to balance the spreading and crystallization processes of PthFu solution, given that the combination of a positive spreading coefficient and a slow solvent evaporation rate is favorable for producing large-area freestanding PthFu nanosheets (Fig.1a and S2). The aggregation and nucleation of polythiophene and fullerene molecules are driven by the π-π stacking, charge-transfer, and hydrophobic interactions.[24] The freestanding pseudo-2D PthFu nanosheets grow in the lateral direction with the dimension of ~ 100 cm^2 on top of the water surface by consuming the remaining thiophene and fullerene molecules (Fig.1b). The spontaneous spreading of PthFu blends effectively controls the packing order of the polymer layer and impedes the oxygen infiltration into the nanosheets. The uniform formation of freestanding PthFu layers can be customized into a variety of structures by conventional cutting methods and transferred onto various artificial substrates (metal foil, paper, glass, polymer, etc., as shown in Fig.1c). The freestanding PthFu nanosheets exhibit high mechanical endurance and strength (discussed in the following section), which enables direct pick-up and rolling for subsequent substrate-free device construction (Fig.1d). The generality of this water-air interfacial growth method has also been shown by successful fabrication of different polymer and molecular systems (Fig.S3-S5).

The optical image of freestanding PthFu nanosheets (Fig. 2a) shows a large-area,

continuous and flat morphology co-occurring with partially folded sheets and wrinkles, indicating the flexibility of the PthFu nanosheet structure. The uniform aberration chromatism throughout the PthFu film implies its homogenous and uniform characteristics, which are further confirmed by scanning electron microscopy (SEM) and atomic force microscopy (AFM) (Fig.S6-S7). The representative high-resolution transmission electron microscopy (HRTEM) and the corresponding selected area diffraction (SAED) pattern images (Fig.2b-c) exhibit a highly crystalline lamellar structure of the freestanding PthFu nanosheet with an interplanar distance of 7.2 Å along the π-π stacking direction [010], and 7.7 Å along the polymer chain direction [001]. X-ray diffraction (XRD, Fig.2d) is employed to gain insight into the molecular packing within the PthFu nanosheet. As shown in Fig.2d, the polythiophene-only nanosheet exhibits four diffraction peaks at 6.79^{o}, 13.63^{o}, 20.43^{o} and 24.63^{o} in the XRD pattern, which correspond to the (100), (200), (300) and (010) planes within an orthorhombic unit cell and lattice constants of a = 13.01 Å, b = 7.22 Å, and c = 7.73 Å. With the incorporation of fullerene molecules, the main diffraction peaks of (100), (200), and (300) are shifted to higher two-theta angles (7.08^{o}, 14.16^{o} and 21.26^{o}), reflecting the changes of lattice constants to a = 12.62 Å, b =7.16 Å, and c = 7.66 Å. The preservation of orthorhombic symmetry in the PthFu nanosheet suggests that its main structure is composed of crystalline polythiophene chains, while the slight modifications of in-plane lattice constants indicate that the fullerene molecules are mainly dispersed along the [100] direction between the adjacent polythiophene domains. Due to the short butyl side-chain of polythiophene, the resulting electrostatic

attractions efficiently increase the pressure on each polymer crystalline domain, thus decreasing the lattice parameters along both [100] and [010] directions. The thickness of PthFu nanosheets from 16 to 600 nm can be controlled by varying the concentration of the spreading solution (Fig.2e). The freestanding pseudo-2D PthFu nanosheets present continuous, smooth and compact film morphologies regardless of its thickness (Inset of Fig. 2e). As shown in Figure 2f, the photoabsorption increases with increasing thickness of the PthFu nanosheets, in which broad near-infrared absorption is observed with a distinct band around 890 nm, attributed to the charge transfer band formation within the PthFu nanosheets (Inset of Fig. 2f).

Given that no C_{60} crystalline domain can be resolved in the PthFu nanosheets, the film conductivities are mainly attributed to the charge transport through the highly ordered polythiophene phase. To investigate the electronic properties of PthFu nanosheets, we measure the vertical thickness and in-plane distance-dependent conductivity along the in-plane and out-of-plane directions (Fig. 3a). The conductivity of both directions gradually decreases non-linearly with the increase of thickness or distance. Meanwhile, the in-plane conductivity exhibits three orders of magnitude larger than that of out-of-plane direction, resulting from the high π-π stacking interaction between the thiophene rings for high carrier mobility along the [010] direction. Furthermore, we perform ab-initio simulations on polymer nanosheets with various thickness (2-4 layers) to further explore the pseudo-2D microscopic structure and to understand its impact on electronic properties. While the atomic configurations inside the slabs

rapidly converge to that of the bulk phase, substantial misalignments between thiophene rings along the π-stacking direction and slight reductions of tilt angles are observed at the surface of the nanosheets (Fig. S9-S11). This can be explained by the suppression of inter-layer steric repulsion at the surface, which is necessary to establish ideal alignment by compensating the intra-layer interactions. Both the broken symmetry and variation of lattice constants for the surface layer compared to bulk crystal slightly modify the energy levels while preserving the dispersion relation (Fig.S11), indicating that the coherent transport along the polythiophene chain is barely affected. By contrast, the transport along the π-stacking direction is more sensitive to the morphology change because the electron coupling is dictated by the thiophene ring alignment (Fig.S9-11). As expected from the strong π-π interactions, the calculated electron coupling along the [100] direction is three orders of magnitude lower than that along the [010] direction, associated with a reduction by a factor of 10^6 in the carrier mobility estimated by the phonon-assisted hopping model (Fig.3b-c). While this is consistent with the more efficient transport along the in-plane direction measured in our experiments (Fig.3a), the small but non-negligible out-of-plane current (3~4 orders of magnitude lower than that of the in-plane direction) is likely to arise from the transport through long polythiophene chains across different domains,[25] rather than direct coupling within the crystalline phase. In addition, the simulations suggest that the electron couplings at the surface of ultra-thin PthFu nanosheets (27~78 meV) are 2.6~7.5 times lower than that inside the bulk phase (~202 meV) as a consequence of the significant structural misalignment, corresponding to a reduction

by a factor of 6.7~55.5 in the hole mobility. Given that the electron couplings inside the 4-layer system already constitute half of the bulk value, the intrinsic transport properties of the polythiophene nanosheets within the thickness range observed in experiments should be identical to the bulk phase. Therefore, the gradual and non-linear decrease of conductivity with increasing thickness and electrode spacing (Fig. 3a) may stem from the variation of defects and grain boundaries.

High charge carrier mobility and broad photoabsorption enable the photovoltaic effect of PthFu nanosheets due to its charge-transfer nature (Fig. S12). The charge-transfer interactions are explored by probing spin-dependent electronic transition in diodes of PthFu nanosheets using electrically detected magnetic resonance spectroscopy (EDMR) for which spin-dependent electric currents are monitored while electron paramagnetic resonance is established with electronic spin states which affect the probed current.[26] The inset of Fig. 3d display both the device structure used for these experiments as well as its asymmetric, diode-like current voltage characteristics. The main panel of Fig. 3d displays a room temperature continuous wave (cw) EDMR spectrum consisting of a plot of the lock-in detected derivative $\frac{\partial \Delta I / I_0}{\partial B} B_m$ of the relative current change as a function of the applied magnetic field B_0 that was recorded in presence of a cw low-power X-band microwave radiation with frequency f = 9.653 GHz using magnetic field modulation with modulation amplitude B_m = 0.1 mT.[27-28] The data reveals the presence of an intrinsic resonance line with peak-to-peak width of ~0.65 mT and a resonance center at a magnetic field corresponding to a

Landé g-factor of g = 2.002(6). The data can be accurately fit by a Gaussian derivative function as expected from paramagnetic electron states which are surrounded by vast proton ensembles that couple to the electron state via anisotropic hyperfine interaction. The existence of an EDMR signals in PthFu nanosheets close to the electron vacuum *g*-factor proves that the charge carrier spin states responsible for these signals are weakly spin-orbit coupled as expected for a material that consists predominantly of period 2 elements. In contrast to EDMR signals found in many other organic semiconductor materials,[29-31] and even many inorganic semiconductors,[32] the EDMR spectrum shown in Fig. 3d does not require the fit with two Gaussian functions. This could either be due to a spin-dependent charge carrier process which involves only one charge carrier species, e.g. a previously hypothesized yet never unambiguously confirmed spin-dependent transport process such as the bipolaron mechanism,[33-34] or, more likely, it could also be due to spin-dependendent electron-hole recombination when both the electron and the hole spin states experience comparable hyperfine field distributions.[35] Most significant about the observation shown in Fig. 3d is the comparatively small magnitude of the observed EDMR signal compared to the EDMR signals found in disordered carbon-based thin films. We attribute the observation of such weak EDMR signals in PthFu nanosheets to the order induced stronger delocalization and higher mobility of charge carriers which possibly shortens both, the mobility limited lifetime of intermediate charge carrier pair states as well as spin-relaxation times. The latter could be caused by a pronounced influence of Elliot Yaffet spin relaxation,[36] that was recently observed in

the crystalline organic semiconductors C_{10}-DNBDT-NW.[37]

The freestanding PthFu nanosheets with high stretchability and mechanical robustness are essential for the development of flexible conformal electronics. The nanoscale mechanical properties of the freestanding PthFu nanosheets are studied by using an ultrafast extreme property mapping (XPM) measurement (Inset of Fig 4a and Fig. S12).[38-39] The indents are performed in a 10*10 grid pattern of freestanding PthFu nanosheets to quickly gather mechanical property distribution statistics and generate spatial distribution maps of localized mechanical properties. The freestanding PthFu nanosheets show an average compressive Young's modulus of 11.3 GPa, which is much larger than that of the spun-cast film of 4.1 GPa (Fig. S13). The consistent nanoscale mechanical features with bulk mechanical testing, together with the modeling analysis (Fig. 4a), confirm the robustness and endurance of freestanding PthFu nanosheets. The Young's modulus is predicted to be 11.0 GPa by density functional theory for the π-stacking direction (Fig. 4a). These results fit the experimental data well, which suggests that the strong π-π interactions and high packing regularity are responsible for the mechanical strength of freestanding PthFu nanosheets (Fig. S14-15). In addition, we investigate the current-voltage (I-V) characteristics of freestanding and mechanical robust PthFu nanosheets with various longitudinal strains, and the results show that the current steadily decreases with increasing strain from 0% to 2.8% (Fig. S16-17). The mechano-electronic properties are further studied by applying a stable and repeatable stress associated with a 0~2.8%

strain variation, which stimulates a steady and periodic current variation maintaining a positive correlation with the source signal (Fig. 4b). A closer examination of the strain-dependent transport in PthFu nanosheets reveals that the conductivity gradually decreases in a linear and monotonic manner with relatively low strain. A transition to nonlinear behavior occurs when the strain exceeds 1.5%, as seen in the drastic drop of conductivity (Fig. 4c).

The DFT simulations are employed to probe the variation of electron coupling and the corresponding change of mobility under different strains (Fig. 4d). Within the scenario of phonon-assisted charge hopping, our model quantitatively reproduces the measured transport suppression in the range of 0.0~1.5% strain. This implies that the decrease of conductivity mainly stems from the homogenous increase of the π-π stacking distance, which substantially reduces the electron coupling and eliminates charge transfer. By contrast, the failure of our simulations to capture the drastic decrease of conductivity beyond 1.5% strain suggests a transition between different structural evolution mechanisms. Interestingly, no critical point associated with such transition is observed in the stress-strain curve, which illustrates the formation of a mechanically connected but electronically disconnected PthFu network. These results in combination with the recoverable behaviors point to the following hypothesis: the breaking down of polymer crystals in some vulnerable sites to incorporate C_{60} molecules becomes energetically favorable when the strain exceeds the critical value. Within such a morphology, the C_{60} molecules serve as effective barriers to block hole

transport due to their large band offsets relative to polythiophene, while preserving the mechanical strength of the system due to their rigid structures. Once the stress is withdrawn, C_{60} molecules tend to aggregate and diffuse to the interstitial area between polymer layers. The *van der Waals* interactions drive the entire process,[40] and the absence of bond breaking and formation may explain the remarkable cycling performance of PthFu networks. This model is consistent with our simulations on a prototype system with sparsely distributed C_{60} molecules sandwiched by layers of polymer crystals (Fig. S18). To further support the above assumptions, a control experiment was performed on polymer-only nanosheets (Inset of Fig. 4c). Similar behavior to that of freestanding PthFu nanosheets is observed with a small strain (<2%), while the trend becomes opposite beyond the critical point, indicating a transition from homogeneous to inhomogeneous stacking.

The extracted Gauge factor of freestanding PthFu nanosheets is calculated from $\pi^{\sigma}=\Delta R/(R*X)$ at the transition region, where ΔR and R are the resistance change and resistance without strain, X is the strain.[41] The freestanding PthFu nanosheets exhibit a high Gauge factor with a value of ~425, which is among the highest in the current strain sensors (Figure 5a).[42-59] The distinct Gauge factor of PthFu nanosheets make them prominent to serve as active materials of strain and pressure sensors. Given the mechanical strength and high flexibility, the freestanding PthFu nanosheets exhibit a robust morphology adjustability to form excellent conformal contacts via wrapping on various target objects with non-planar surfaces.[60-61] We utilize the excellent

conformability of freestanding PthFu nanosheets with the target object to explore pressure and temperature sensors for detecting the stimuli variation in an artificial blood-vessel-like rubber tubing (Fig. 5b-c). With the tube expanded by blowing an external gas, the induced strain can be sufficiently transferred to the freestanding PthFu nanosheet, whereas the temperature sensor is based on the increase of phonon density with increasing temperature that facilitates charge transport. By monitoring the pressure-dependent current change, the substrate-free PthFu sensors show the precision with less than 5% uncertainty (Fig. 5d), as compared to 15% of the Polydimethylsiloxane (PDMS) substrate-coated PthFu sensor. Figure 5e shows the pressure-dependent relative current change of PthFu nanosheets with and without the substrate on the artificial blood vessel, on which the relative current change is un-proportional to the substrate thickness, indicating the higher sensitivity of substrate-free PthFu nanosheet sensor. In addition, because of the substrate acting as a buffer layer, the induced strain cannot be sufficiently transferred to the PthFu nanosheet, and therefore the response time of real-time pressure monitoring increases with the substrate thickness (Fig. S19).

Due to its conformability and flexibility, the substrate-free PthFu sensor can be adapted to objects with extremely rough surfaces for real-time temperature monitoring (Fig. 6a and Fig. S20). Provided a target object full of small wrinkles (1 mm between the adjacent wrinkles), the substrate-free PthFu nanosheet can adhere tightly to the wrinkled surface (Fig. 6b) as the conformal sensing systems, while the

substrate-coated PthFu nanosheet does not allow the conformal attachment (Fig. 6b). As the temperature increases, the charge transport rate increases in PthFu nanosheet, leading to an enhanced current output (Fig. 6c). Under the same temperature variation, the substrate-free conformal sensor shows a more substantial current change due to its surface adaptability than that of sensors with the substrate. In addition, a delayed response time is observed for the temperature sensor with the substrate, indicating its lower sensitivity (Fig. 6c). This can be attributed to 1) thermal gradient between the top and bottom sites of the wrinkles, and 2) the heat transfer blocking effect with the extra substrate. The temperature dependent current change (inset of Fig. 6d) can monitor the real-time temperature variation of the target object. The substrate-free PthFu sensor can accurately detect the temperature variation of the rough surface object reversibly heated or cooled from 298 K to 320 K, while the temperature obtained by the substrate-coated PthFu sensor is much lower than the real temperature variation (Fig. 6d). In addition, a significant uncertainty emerges for the non-planar surfaces using the substrate-coated sensor with ~1.5 s of delay time, while the response time is ~ 0.1 ms for substrate-free conformal sensor. The substrate-free freestanding PthFu nanosheet sensors exhibit high precision and the real-time sensitivity, responding to the external thermal and pressure stimuli.

In conclusion, a scalable and versatile water-air assembly method is developed to grow freestanding crystalline conjugated polymer PthFu nanosheets. Desired mechanical strength, high flexibility, and efficient charge transport are simultaneously

achieved in PthFu nanosheets, which are found to stem from the substantial nanoconfinement effect that augments the synergy between crystalline domains and packing order. The intrinsic linkages between mechanical, electronic, thermal, and magnetic responses stem from the same structural evolution of pseudo-2D PthFu nanosheets, and thus establish exceptional responses to a variety of external stimuli. The potential of designing substrate-free devices based on crystalline polymer PthFu nanosheets is demonstrated by our success in accurately detecting the temperature/pressure with little hysteresis. The possibility of extending the built-in functionalities is further illustrated by coupling photovoltaic module to existing sensor responses. The unique features of freestanding polymer nanosheets make them especially promising for a range of in-situ monitoring and wearable applications.

References:

1. Darwish, A.; Hassanien, A. E. *Sensors* **2011,** 11, 5561-5595.

2. Patel, M.; Wang, J. Applications, challenges, and prospective in emerging body area networking technologies. *IEEE Wireless communications* **2010,** 17, 10.

3. Jeong, C. K.; Park, K.-I.; Son, J. H.; Hwang, G.-T.; Lee, S. H.; Park, D. Y.; Lee, H. E.; Lee, H. K.; Byun, M.; Lee, K. J. *Energy Environ. Sci.* **2014,** 7, 4035-4043.

4. Toivola, M.; Ferenets, M.; Lund, P.; Harlin, A. *Thin Solid Films* **2009,** 517, 2799-2802.

5. Pang, C.; Lee, C.; Suh, K. Y. *J. Appl. Polym. Sci.* **2013,** 130, 1429-1441.

6. Sirringhaus, H.; Brown, P.; Friend, R.; Nielsen, M. M.; Bechgaard, K.; Langeveld-Voss, B.; Spiering, A.; Janssen, R. A.; Meijer, E.; Herwig, P. *Nature* **1999,** 401, 685-688.

7. Sirringhaus, H.; Tessler, N.; Friend, R. H. *Science* **1998,** 280, 1741-1744.

8. Xu, J.; Wang, S.; Wang, G.-J. N.; Zhu, C.; Luo, S.; Jin, L.; Gu, X.; Chen, S.; Feig, V. R.; To, J. W. *Science* **2017,** 355, 59-64.

9. Si, L.; Massa, M. V.; Dalnoki-Veress, K.; Brown, H. R.; Jones, R. A. *Phys. Rev. Lett.* **2005,** 94, 127801.

10. Ellison, C. J.; Torkelson, J. M. *Nat. Mater.* **2003,** 2, 695-700.

11. Shin, K.; Woo, E.; Jeong, Y. G.; Kim, C.; Huh, J.; Kim, K.-W. *Macromolecules* **2007,** 40, 6617-6623.

12. Keddie, J. L.; Jones, R. A.; Cory, R. A. *Europhys. Lett.* **1994,** 27, 59.

13. Stafford, C. M.; Vogt, B. D.; Harrison, C.; Julthongpiput, D.; Huang, R.

Macromolecules **2006,** 39, 5095-5099.

14. Zheng, Z.; Yim, K.-H.; Saifullah, M. S.; Welland, M. E.; Friend, R. H.; Kim, J.-S.; Huck, W. T. *Nano lett.* **2007,** 7, 987-992.

15. Aryal, M.; Trivedi, K.; Hu, W. *ACS nano* **2009,** 3, 3085-3090.

16. Ma, W.; Yang, C.; Gong, X.; Lee, K.; Heeger, A. J. *Adv. Funct. Mater.* **2005,** 15, 1617-1622.

17. Kim, J. Y.; Lee, K.; Coates, N. E.; Moses, D.; Nguyen, T.-Q.; Dante, M.; Heeger, A. J. *Science* **2007,** 317, 222-225.

18. Kim, Y.; Cook, S.; Tuladhar, S. M.; Choulis, S. A.; Nelson, J.; Durrant, J. R.; Bradley, D. D.; Giles, M.; McCulloch, I.; Ha, C.-S. *Nat. Mater.* **2006,** 5, 197-203.

19. Zhang, Z.; Li, P.F.; Tang, Y.Y.; Wilson, A.J.; Willets, K.; Wuttig, M.; Xiong, R.G.; Ren, S. *Sci. Adv.* **2017,** 3, e1701008.

20. Kunieda, M.; Liang, Y.; Fukunaka, Y.; Matsuoka, T.; Takamura, K.; Loahardjo, N.; Winoto, W.; Morrow, N. R. *Energy Fuels* **2012,** 26, 2736-2741.

21. Dussaud, A. D.; Troian, S. M. Dynamics of spontaneous spreading with evaporation on a deep fluid layer. *Phys. Fluids* **1998,** 10, 23-38.

22. Krishnakumar, P., Wetting and spreading phenomena. Physics: 2010.

23. Zhang, Z.; Remsing, R.C.; Chakraborty, H.; Gao, W.; Yuan, G.; Klein, M.L.; Ren, S. *Proc. Natl. Acad. Sci. U.S.A.* **2018,** 115, 3776-3781.

24. Zhang, Z.; Li, H.; Luo, Z.; Chang, S.; Li, Z.; Guan, M.; Zhou, Z.; Liu, M.; Grossman, J.C.; Ren, S. *Chem. Mater.* **2017,** 29, 9851-9858.

25. Noriega, R.; Rivnay, J.; Vandewal, K.; Koch, F. P.; Stingelin, N.; Smith, P.; Toney,

M. F.; Salleo, A. *Nat. Mater.* **2013,** 12, 1038.

26. Boehme, C.; Malissa, H. *eMagRes* **2017**.

27. Lee, S.-Y.; Paik, S.; McCamey, D. R.; Boehme, C. *Phys. Rev. B* **2012,** 86, 115204.

28. Waters, D.; Joshi, G.; Kavand, M.; Limes, M.; Malissa, H.; Burn, P.; Lupton, J.; Boehme, C. *Nat. Phys.* 2015, 11, 910-914.

29. Miller, R.; Van Schooten, K.; Malissa, H.; Joshi, G.; Jamali, S.; Lupton, J.; Boehme, C. *Phys. Rev. B* 2016, 94, 214202.

30. Van Schooten, K. J.; Baird, D. L.; Limes, M. E.; Lupton, J. M.; Boehme, C. *Nat. Commun.* **2015,** 6, 6688.

31. Morishita, H.; Baker, W.; Waters, D.; Baarda, R.; Lupton, J.; Boehme, C. *Phys. Rev. B* **2014,** 89, 125311.

32. Herring, T.; Lee, S.-Y.; McCamey, D.; Taylor, P.; Lips, K.; Hu, J.; Zhu, F.; Madan, A.; Boehme, C. *Phys. Rev. B* **2009,** 79, 195205.

33. Behrends, J.; Schnegg, A.; Lips, K.; Thomsen, E.; Pandey, A. K.; Samuel, I.; Keeble, D. *Phys. Rev. Lett.* **2010,** 105, 176601.

34. Boehme, C.; Lupton, J. M. *Nat. Nanotechnol.* **2013,** 8, 612-615.

35. McCamey, D.; Van Schooten, K.; Baker, W.; Lee, S.-Y.; Paik, S.-Y.; Lupton, J.; Boehme, C. *Phys. Rev. Lett.* **2010,** 104, 017601.

36. Boehme, C. *Nat. Phys.* **2017,** 13, 928-929.

37. Tsurumi, J.; Matsui, H.; Kubo, T.; Häusermann, R.; Mitsui, C.; Okamoto, T.; Watanabe, S.; Takeya, J. *Nat. Phys.* **2017,** 13, 994-998.

38. Zhang, Z.; Lee, N.; Patel, K.; Young, M.; Zhang, J.; Percec, S.; Ren, S. *Adv. Eng.*

Mater. **2018,** 20, 1800095.

39. Zhang, Z.; Mogurampelly, S.; Percec, S.; Hu, Y.; Fiorin, G.; Klein, M.L.; Ren, S. *J. Phys. Chem. Lett.* **2018**, 9, 2652–2658.

40. Zhang, Z.; Li, H.; Luo, Z.; Chang, S.; Li, Z.; Guan, M.; Zhou, Z.; Liu, M.; Grossman, J.C.; Ren, S. *Chem. Mater.* **2017,** 29, 9851-9858.

41. Yang, S.; Lu, N. *Sensors* **2013,** 13, 8577-8594.

42. Yao, S.; Zhu, Y. *Nanoscale* **2014,** 6, 2345-2352.

43. Lee, J.; Kim, S.; Lee, J.; Yang, D.; Park, B. C.; Ryu, S.; Park, I. *Nanoscale* **2014,** 6, 11932-11939.

44. Amjadi, M.; Pichitpajongkit, A.; Lee, S.; Ryu, S.; Park, I. *ACS nano* **2014,** 8, 5154-5163.

45. Boland, C. S.; Khan, U.; Backes, C.; O'Neill, A.; McCauley, J.; Duane, S.; Shanker, R.; Liu, Y.; Jurewicz, I.; Dalton, A. B. *ACS nano* **2014,** 8, 8819-8830.

46. Hempel, M.; Nezich, D.; Kong, J.; Hofmann, M. *Nano lett.* **2012,** 12, 5714-5718.

47. Tian, H.; Shu, Y.; Cui, Y.-L.; Mi, W.-T.; Yang, Y.; Xie, D.; Ren, T.-L. *Nanoscale* **2014,** 6, 699-705.

48. Zhao, J.; He, C.; Yang, R.; Shi, Z.; Cheng, M.; Yang, W.; Xie, G.; Wang, D.; Shi, D.; Zhang, G. *Appl. Phys. Lett.* **2012,** 101, 063112.

49. Wang, Y.; Wang, L.; Yang, T.; Li, X.; Zang, X.; Zhu, M.; Wang, K.; Wu, D.; Zhu, H. *Adv. Funct. Mater.* **2014,** 24, 4666-4670.

50. Fu, X.-W.; Liao, Z.-M.; Zhou, J.-X.; Zhou, Y.-B.; Wu, H.-C.; Zhang, R.; Jing, G.; Xu, J.; Wu, X.; Guo, W. *Appl. Phys. Lett.* **2011,** 99, 213107.

51. Xiao, X.; Yuan, L.; Zhong, J.; Ding, T.; Liu, Y.; Cai, Z.; Rong, Y.; Han, H.; Zhou, J.; Wang, Z. L. *Adv. Mater.* **2011,** 23, 5440-5444.

52. Liu, N.; Fang, G.; Wan, J.; Zhou, H.; Long, H.; Zhao, X. *J. Mater. Chem.* **2011,** 21, 18962-18966.

53. Roh, E.; Hwang, B.-U.; Kim, D.; Kim, B.-Y.; Lee, N.-E. *ACS nano* **2015,** 9, 6252-6261.

54. Slobodian, P.; Riha, P.; Benlikaya, R.; Svoboda, P.; Petras, D. A *IEEE Sens. J.* **2013,** 13, 045-4048.

55. Cohen, D. J.; Mitra, D.; Peterson, K.; Maharbiz, M. M. *Nano Lett.* **2012,** 12, 1821-1825.

56. Cai, L.; Song, L.; Luan, P.; Zhang, Q.; Zhang, N.; Gao, Q.; Zhao, D.; Zhang, X.; Tu, M.; Yang, F. *Sci. Rep.* **2013,** 3, 3048.

57. Lipomi, D. J.; Vosgueritchian, M.; Tee, B. C.; Hellstrom, S. L.; Lee, J. A.; Fox, C. H.; Bao, Z. *Nat. Nanotechnol.* **2011,** 6, 788-792.

58. Yamada, T.; Hayamizu, Y.; Yamamoto, Y.; Yomogida, Y.; Izadi-Najafabadi, A.; Futaba, D. N.; Hata, K. *Nat. Nanotechnol.* **2011,** 6, 296-301.

59. Tadakaluru, S.; Thongsuwan, W.; Singjai, P. *Sensors* **2014,** 14, 868-876.

60. Zang, Y.; Zhang, F.; Di, C.-a.; Zhu, D. *Mater. Horiz.* **2015,** 2, 140-156.

61. Pang, C.; Lee, G.-Y.; Kim, T.-i.; Kim, S. M.; Kim, H. N.; Ahn, S.-H.; Suh, K.-Y. A *Nat. Mater.* **2012,** 11, 795.

ASSOCIATED CONTENT

Supporting information. The following file is available free of charge.

(1) Experimental Section, (2) Synthesis process and morphology of the picked-up film, (3) Anisotropic electronic properties in bulk P3BT crystals, (4) Surface effects in 2D P3BT nanosheets, (5) Photoelectric properties of PthFu nanosheets, (6) Mechanical and Mechano-electronic properties of PthFu nanosheets, (7) PthFu film based conformal temperature sensors.

Acknowledgements

Work at the University at Buffalo (S.R.) was supported by the U.S. Department of Energy, Office of Basic Energy Sciences, Division of Materials Sciences and Engineering under Award DE-SC0018631. This research used resources of the National Energy Research Scientific Computing Center, a DOE Office of Science User Facility supported by the Office of Science of the U.S. Department of Energy under Contract No. DE-AC02-05CH11231. The electrically detected magnetic resonance experiments (C. B) were supported by the US Department of Energy, Office of Basic Energy Sciences, Division of Materials Sciences and Engineering under Award #DE-SC0000909. We also thank the support from National Supercomputer Center in Guangzhou on computational resources.

Author Contributions

Z. Z and H. L. contributed equally in this paper. Z. Z carried out experiments and wrote the paper. H. L. conducted the theoretical calculation. R. M., S. J. and H. M.

collected and analyzed the electrically detected magnetic resonance spectroscopy data. S. R., J. G. and C. B. lead the project. All authors discussed the results and commented on the manuscript.

Competing financial interests.

The authors declare no competing financial interest.

Figure Captions

Figure 1. Schematic illustration of the formation and transferring process of freestanding polythiophene-fullerene (PthFu) nanosheets. (a) Schematic illustration of self-assembly approach to grow mechanically strong and freestanding polymer PthFu nanosheets at the water-air interface. The solution spreading mechanism of freestanding PthFu nanosheets described by the Neumann triangle of force (Fig. S1). (b) Four sequential stages during the self-assembly procedure. (i) Solvent of positive spreading coefficient with organic solutes spreading on water. (ii) Solvent evaporation induced nucleation. (iii) Self-assembly for the formation of PthFu nanosheets. (iv) As-prepared nanosheets growing on water. (c) A typical transferring method for the as prepared PthFu nanosheets with various substrates, e.g. aluminum foil, paper, indium tin oxide (ITO) glass and polydimethylsiloxane (PDMS). (d) A typical transferring of the freestanding PthFu nanosheets without substrates by directly picking up. The lightweight flexible PthFu nanosheets can be easily rolled and unfolded.

Figure 2. Morphology, structure characteristics of PthFu nanosheets. (a) Optical image of typical PthFu nanosheets. (b) High resolution TEM image of highly crystalline PthFu nanosheets. Inset shows the typical TEM images of the freestanding PthFu nanosheets with large-area, continuous and flat morphology co-occurring with partially folded sheets and wrinkles. (c) The SAED pattern recorded along [100] direction. (d) XRD patterns of freestanding PthFu film and spin-coated polythiophene film. (e) Concentration controlled thickness-dependent films. The inset shows the

films with typical thickness of 16 nm, 120 nm, and 300 nm, where the ultrathin film was transitioned from transparent to opaque as the thickness getting thicker. The corresponding AFM images exhibit continuous, smooth and compact film morphology. (f) Absorption spectrums of PthFu nanosheets with different thickness. The inset shows the charge transfer induced absorption band.

Figure 3. Electronic property of PthFu nanosheets. (a) Measured conductivities along the out-of-plane and in-plane directions with various heights and distances of PthFu films. (b) Electron couplings between neighboring polymers along the π-stacking direction for bulk polythiophene crystal and polythiophene nanosheets containing 2-4 layers computed by the anti-crossing method, with the thiophene ring alignments shown in the inset. The labels "inner" and "outer" denote the positions inside and at the surface of the nanosheets, respectively. (c) Calculated electron couplings between polymers with different configurations (cf1 and cf2) along the [100] direction. (d) Electrically detected magnetic resonance spectra from PthFu nanosheet diodes. The figure shows a continuous wave EDMR spectra. For experimental details see text. A sketch of the used device structure is shown in the top left inset, the bias voltage to the PthFu layer is applied between the top contact (Al/Ca) and the bottom contact (indium tin oxide). The current-voltage characteristic of the resulting diode is shown in the top right inset.

Figure 4. Mechanical and mechano-electronic properties of PthFu nanosheets. (a)

Calculated stress-strain curves for bulk polythiophene crystal along the [010] and [001] directions, with the linearly fitting presented in straight lines. Inset: The XPM images of the freestanding PthFu nanosheet. (b) Time dependent strain, and current variations of PthFu nanosheets. (c) Conductivity change as a function of tensile strain of PthFu nanosheets. Inset shows the conductivity change as a function of tensile strain of polythiophene film. (d) Computed strain dependent electron coupling (V) and carrier mobility (μ) reduction.

Figure 5. Strain/Pressure conformal sensors based on freestanding PthFu nanosheets. (a) The Gauge factor of the strain sensors in this work and in the literatures. (b) Schematic illustrations of the strain/pressure sensor with the inset showing the photograph of the PthFu nanosheet directly wrapping on the artificial blood vessel. (c) Schematic illustrations of the mechanism of strain/pressure sensor. The pressure in the vessel expand the vessel wall and the stain results in the lattice expansion of the outside PthFu nanosheet, which decreases the charge transport rate along π-stacking direction. (d) Time dependent relative current change of the freestanding PthFu nanosheet at various pressure from 1.3 kPa to 5.5 kPa. (e) Pressure dependent relative current change of the PthFu nanosheet on flexible polydimethylsiloxane (PDMS) substrate with various thickness.

Figure 6. Temperature conformal sensors based on freestanding PthFu nanosheets. (a-b) Schematic illustrations of the temperature sensors with and without PDMS

substrate, where the temperature sensor without PDMS substrate can be well adapted on target with rough surface full of small wrinkles. (c) Time dependent relative current change of the PthFu nanosheet based temperature sensors with and without PDMS substrate. (d) Real time temperature monitoring of the PthFu nanosheet based temperature sensors with and without PDMS substrate. The time dependent temperature values were obtained from time dependent relative current change (Fig. 6c) and intrinsic temperature dependent relative current change (Inset of Fig. 6d).

Figure 1

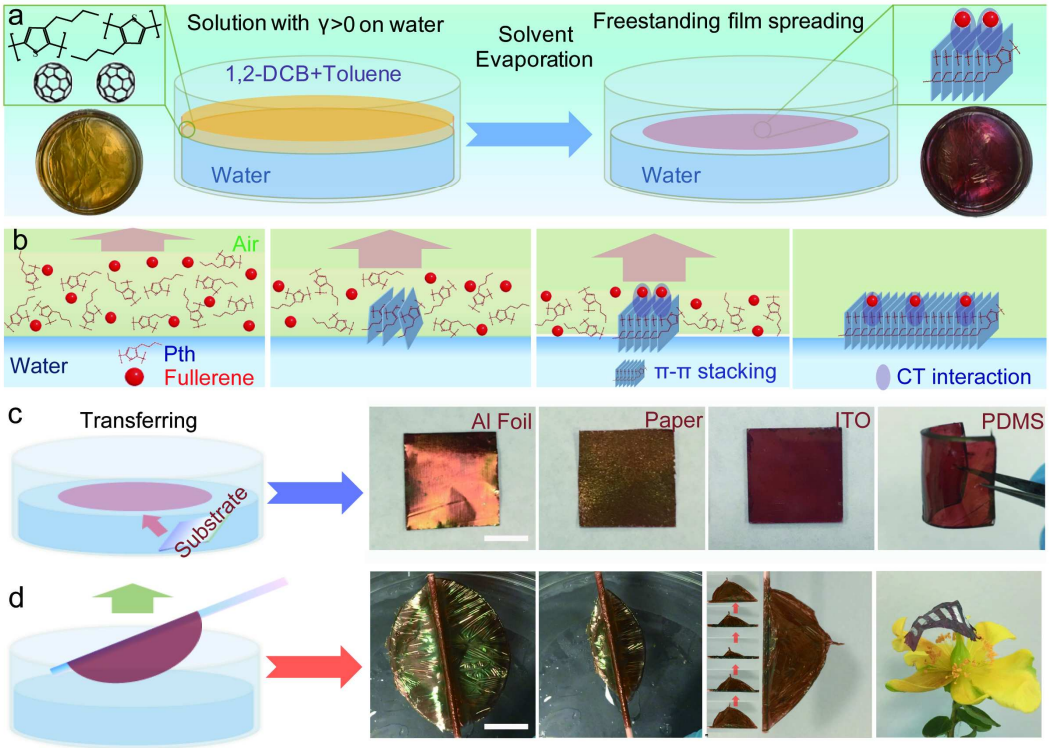
a
Solution with γ>0 on water
1,2-DCB+Toluene
Water
Solvent Evaporation
Freestanding film spreading
Water
b
Air
Water
Pth
Fullerene
π-π stacking
CT interaction
c
Transferring
Substrate
Al Foil
Paper
ITO
PDMS
d

Figure 2

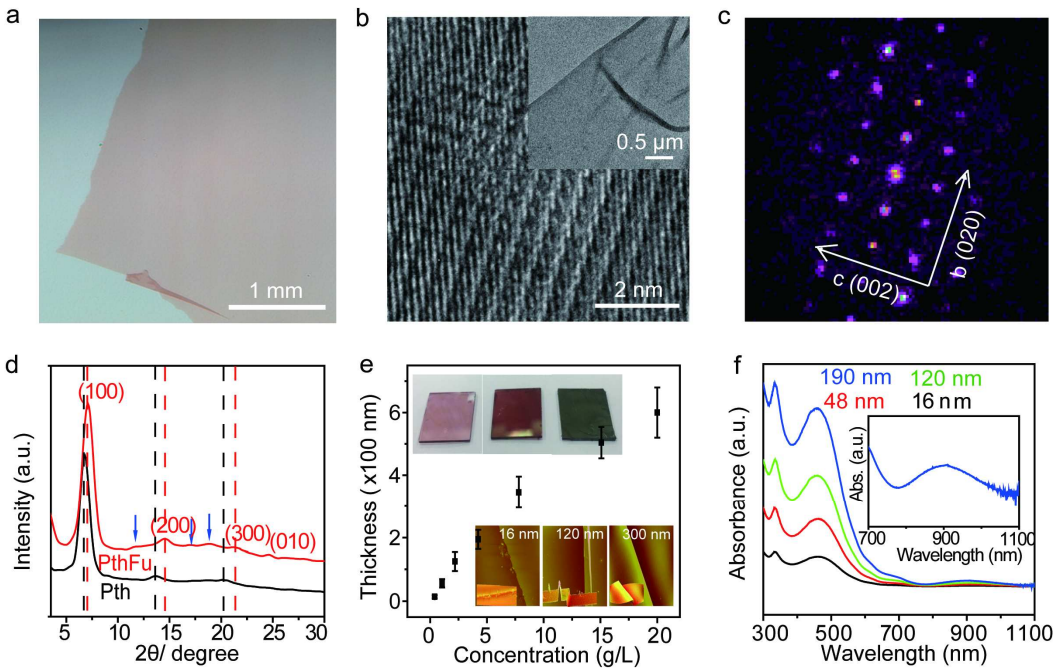
a
1 mm
b
0.5 μm
2 nm
c
c (002)
b (020)
d
(100)
(200)
(300)
(010)
PthFu
Pth
Intensity (a.u.)
2θ/ degree
e
Thickness (x100 nm)
Concentration (g/L)
16 nm
120 nm
300 nm
f
190 nm
120 nm
48 nm
16 nm
Absorbance (a.u.)
Abs. (a.u.)
Wavelength (nm)

Figure 3

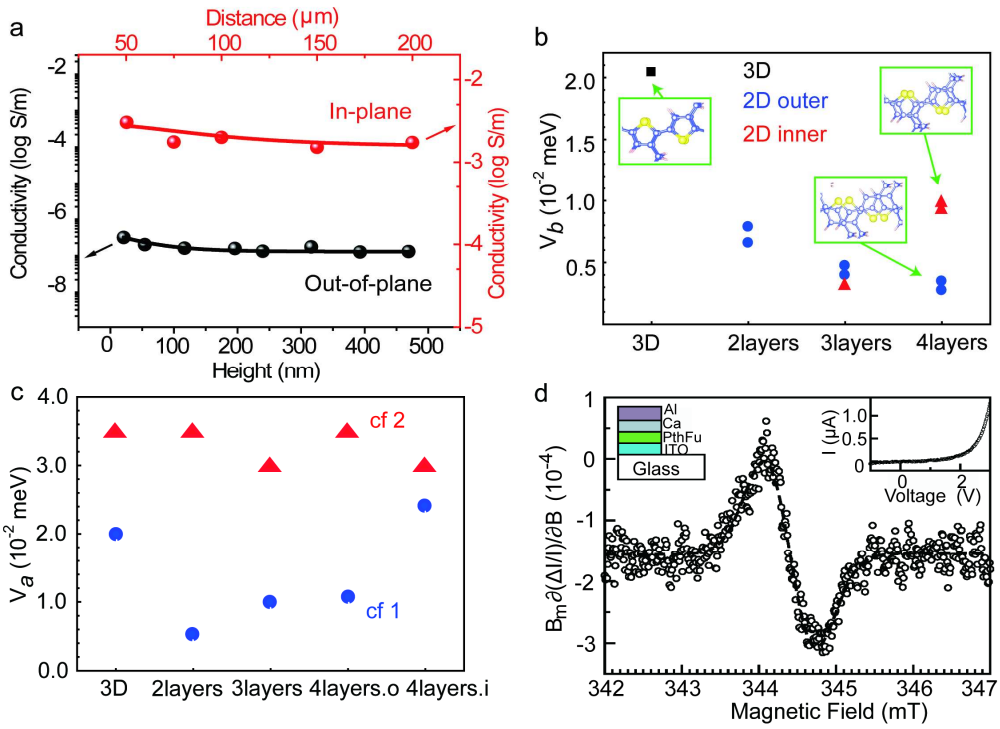
a
Distance (μm)
50
100
150
200
Conductivity (log S/m)
In-plane
Out-of-plane
Conductivity (log S/m)
Height (nm)
b
3D
2D outer
2D inner
V_b (10^{-2} meV)
3D
2layers
3layers
4layers
c
cf 2
cf 1
V_a (10^{-2} meV)
3D
2layers
3layers
4layers.o
4layers.i
d
Al
Ca
PthFu
ITO
Glass
I (μA)
Voltage (V)
$B_m\partial(\Delta I/I)/\partial B$ (10^{-4})
Magnetic Field (mT)

Figure 4

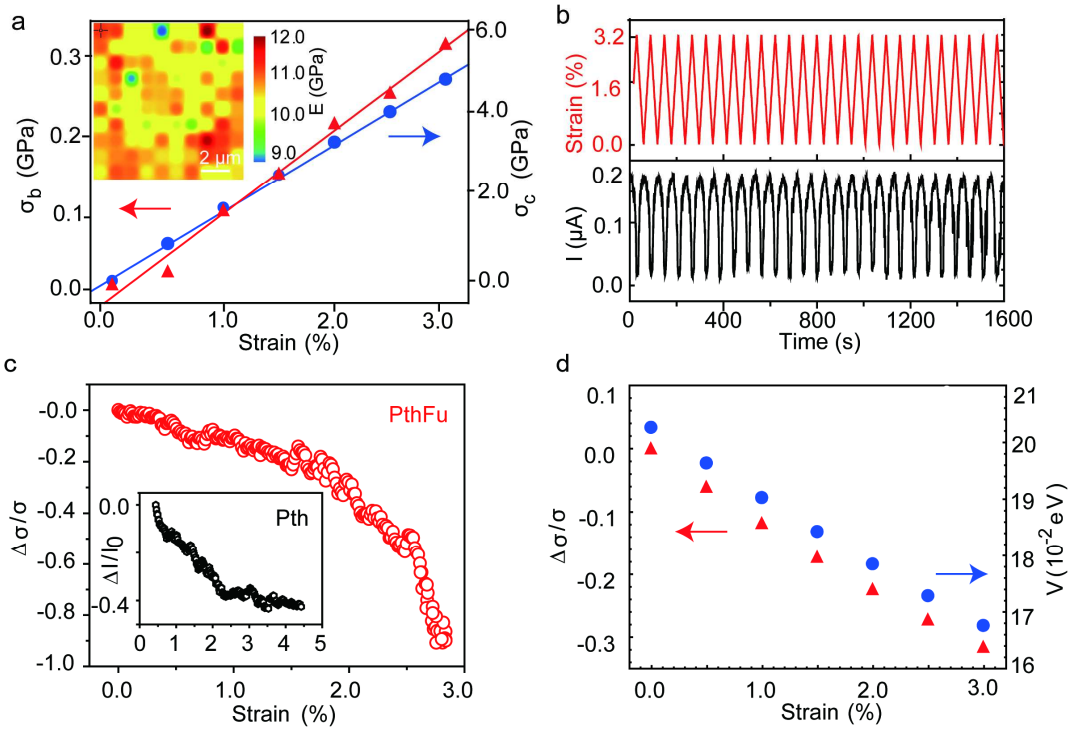
a
b
c
d
σb (GPa)
σc (GPa)
E (GPa)
12.0
11.0
10.0
9.0
2 μm
Strain (%)
Strain (%)
I (μA)
Time (s)
PthFu
Pth
Δσ/σ
ΔI/I0
Strain (%)
Δσ/σ
V (10-2 eV)
Strain (%)

Figure 5

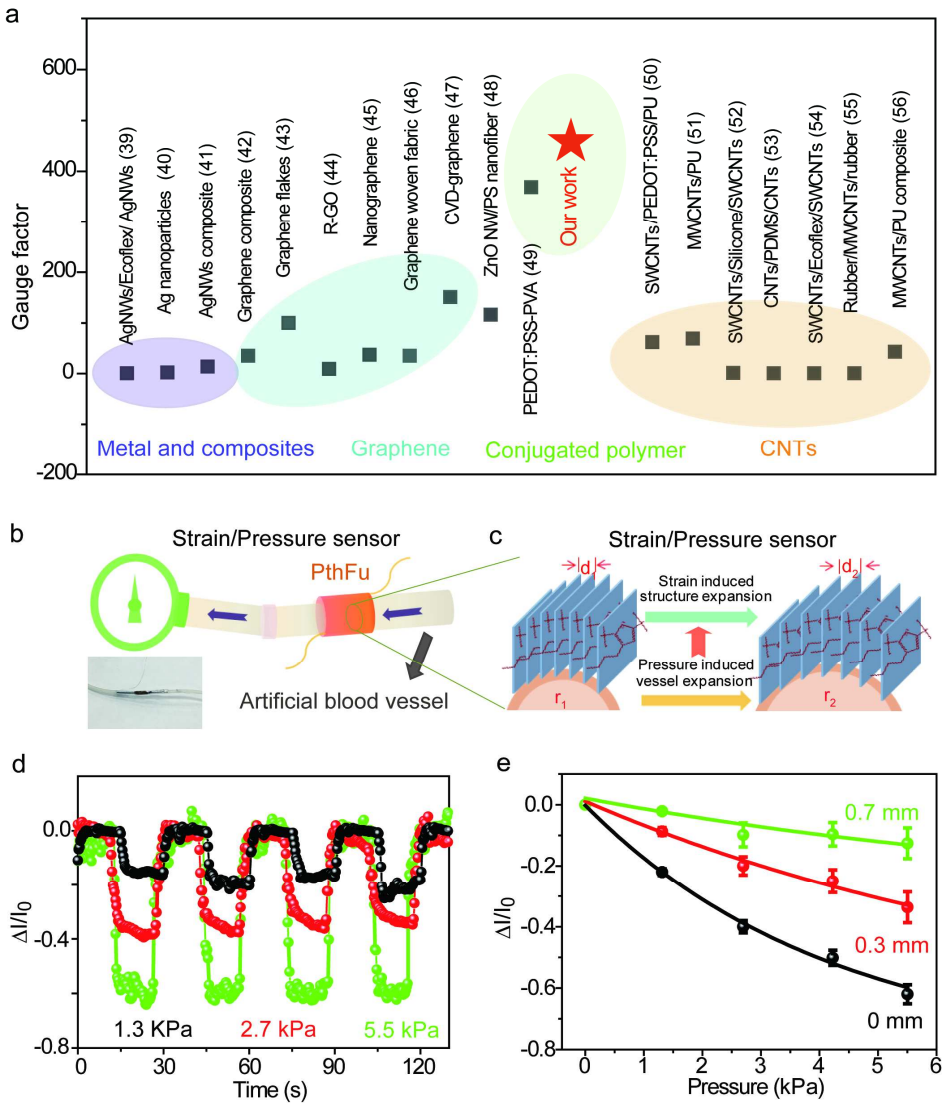
a
Gauge factor
600
400
200
0
-200
AgNWs/Ecoflex/ AgNWs (39)
Ag nanoparticles (40)
AgNWs composite (41)
Graphene composite (42)
Graphene flakes (43)
R-GO (44)
Nanographene (45)
Graphene woven fabric (46)
CVD-graphene (47)
ZnO NW/PS nanofiber (48)
PEDOT:PSS-PVA (49)
Our work
SWCNTs/PEDOT:PSS/PU (50)
MWCNTs/PU (51)
SWCNTs/Silicone/SWCNTs (52)
CNTs/PDMS/CNTs (53)
SWCNTs/Ecoflex/SWCNTs (54)
Rubber/MWCNTs/rubber (55)
MWCNTs/PU composite (56)
Metal and composites
Graphene
Conjugated polymer
CNTs
b
Strain/Pressure sensor
PthFu
Artificial blood vessel
c
Strain/Pressure sensor
d1
Strain induced structure expansion
Pressure induced vessel expansion
d2
r1
r2
d
ΔI/I0
0.0
-0.4
-0.8
1.3 KPa
2.7 kPa
5.5 kPa
0
30
60
90
120
Time (s)
e
ΔI/I0
0.0
-0.2
-0.4
-0.6
-0.8
0.7 mm
0.3 mm
0 mm
0
1
2
3
4
5
6
Pressure (kPa)

Figure 6

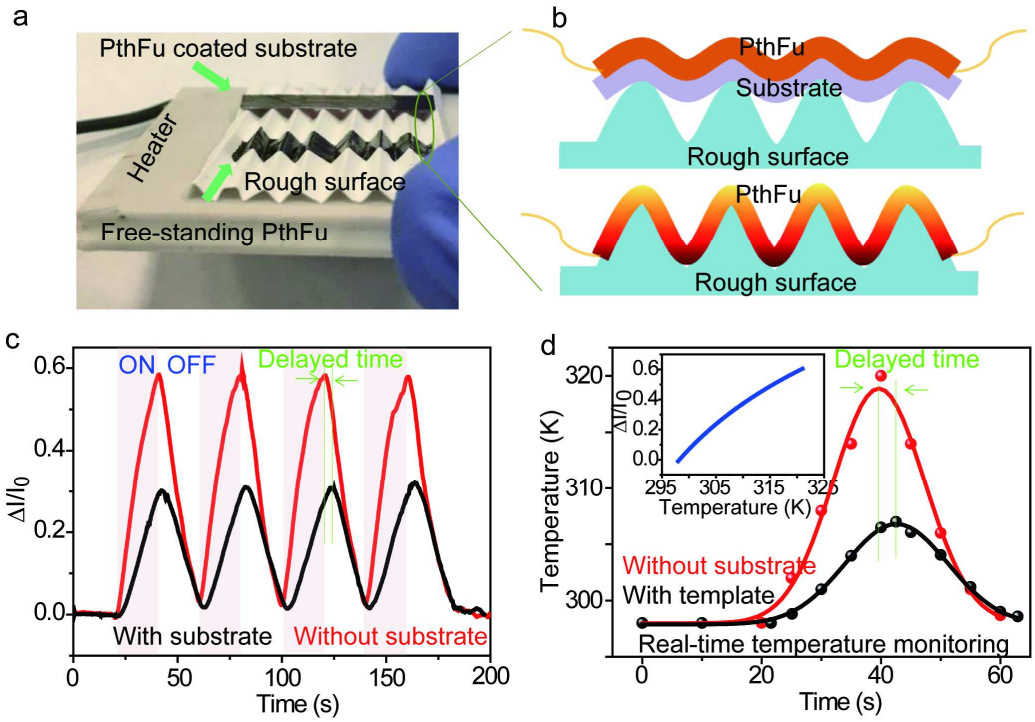
a
PthFu coated substrate
Heater
Rough surface
Free-standing PthFu
b
PthFu
Substrate
Rough surface
PthFu
Rough surface
c
ON OFF
Delayed time
ΔI/I0
With substrate
Without substrate
Time (s)
d
Delayed time
Temperature (K)
ΔI/I0
Temperature (K)
Without substrate
With template
Real-time temperature monitoring
Time (s)

TOC

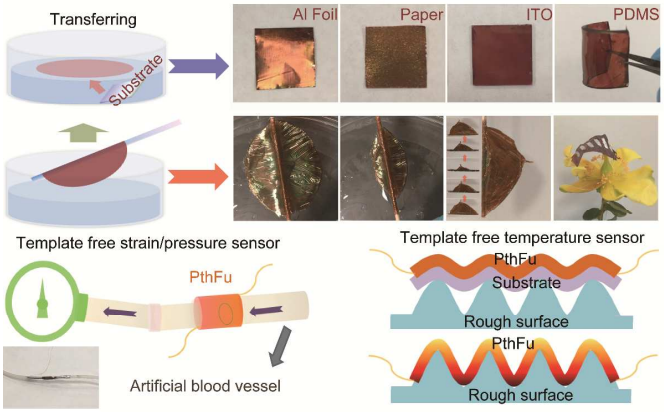
Transferring
Substrate
Al Foil
Paper
ITO
PDMS
Template free strain/pressure sensor
PthFu
Artificial blood vessel
Template free temperature sensor
PthFu
Substrate
Rough surface
PthFu
Rough surface